Nuclear Instruments and Methods in Physics Research A 335 (1993) 44–58
North-Holland

NUCLEAR INSTRUMENTS & METHODS IN PHYSICS RESEARCH
Section A

Spatial resolution of silicon microstrip detectors

R. Turchetta
LEPSI, ULP / CNRS. Strasbourg, France

Received 19 March 1993 and in revised form 14 June 1993

The spatial resolution of silicon microstrip detectors is studied as a function of the main detector parameters and of the track angle. Several algorithms for finding the position of particle hits are presented and analysed. Analytic expressions of the spatial resolution are derived for the main algorithms. Using a Monte Carlo simulation, the spatial resolution is calculated for each algorithm and, for each detector design and track geometry, the algorithm that gives the best resolution is determined.

1. Introduction

Silicon microstrip detectors are widely used as precise vertex detectors in both fixed target and collider high energy physics experiments [1–4]. For tracks impinging the detector along a line perpendicular to the detector surface (0° tracks, see fig. 2), spatial resolution of less than 1.8 μm [5] has been measured, using a 25 μm pitch detector. In recent years, a growing interest has been expressed in the measurement of the spatial resolution for non-perpendicular (inclined) tracks [6–9]. This interest is related to the development of collider vertex detectors based on double-sided microstrip detectors, where particles traverse the detector at large angle ϑ. For example in DELPHI, tracks with an angle of up to 45° are detected in the Microvertex upgrade project with double-sided detectors, and in the Forward Barrel Microvertex project tracks could traverse the detector at angles larger than 70° [10]. A similar situation is likely to be found in future collider vertex detectors [11,12].

In this paper, we discuss the limits on the spatial resolution for different detector configurations and for a wide angular range, from 0 to 75°. Different algorithms are considered and compared using a Monte Carlo simulation (section 2). In sections 3 and 4, the best algorithms for perpendicular and inclined tracks respectively are presented, and their spatial resolution is thoroughly analysed. In section 5, the behaviour of spatial resolution with respect to the different detector parameters and to the geometry of the tracks is discussed, and our results are compared to the available experimental data. Our analysis shows that for each given set of track angle and detector parameters, a particular algorithm must be chosen in order to fully exploit the resolution of silicon microstrip detectors.

2. Monte Carlo simulation

2.1. The construction of the charge signal

In the Monte Carlo simulation, only the total charge measured by the charge preamplifiers is calculated. The analytic expression of the electric field in a planar abrupt p–n junction [13] is used. In the construction of the charge signal at the output of the preamplifier, we can distinguish four phases.

2.1.1. Charge generation

The minimum ionizing particle (MIP) traversing the silicon loses energy that goes into the generation of electron–hole pairs at the mean ratio of 3.7 eV per pair. In the simulation, energy loss is calculated independently in each slice of 10 μm of path in silicon according to the corresponding Landau distribution (most probable energy loss equal to 2.1 keV), convoluted with a Gaussian of standard deviation

$$\sigma = \sqrt{t_{\text{slice}}\delta_2},$$

where $\delta_2 = 1000$ keV^2/cm, and $t_{\text{slice}} = 10$ μm. The value of δ_2 has been chosen in order to have the correct value of the most probable energy loss for a thickness of 300 μm. No delta ray production has been considered.

2.1.2. Charge drift and diffusion

A drift time t_d is calculated for each 10 μm slice; this time depends on the slice position as well as on the type of carriers we are considering: junction side (p-side) strips collect holes, while ohmic side (n-side) strips collect electrons. For each slice, diffusion is considered to be exactly Gaussian, i.e. the charge clouds arriving at the strips is a Gaussian with a standard

deviation given by

$$\sigma_{\text{diff}} = \sqrt{2Dt_{\text{d}}},$$

where D is the diffusion coefficient.

2.1.3. Capacitive coupling

After steps 2.1.1 and 2.1.2, a total charge signal arriving at the strips can be calculated by summing up the individual contributions of each 10 μm slice. For each strip, the fraction of the signal that is detected by the corresponding amplifier depends on the equivalent electrical network of the detector. Strip-to-backplane capacitance can be neglected, since its value is about 10 times smaller than interstrip capacitance C_{IS} in most of the geometry [14,15]. This means losses of signal towards the backplane are not considered. The capacitance of a strip towards next-to-the-closest neighbours can be neglected since it is usually quite smaller than the capacitance of a strip towards closest neighbours [14]. In AC-coupled detectors [16], a decoupling capacitance C_{DEC} is integrated between the strip and the readout electronics. The equivalent electrical network is shown in fig. 1. A simple calculation shows that a fraction K of the charge arriving at one strip appears at the output of the neighbouring amplifiers. This fraction is given by

$$K = \frac{C_{\text{NEI}}}{C_{\text{DEC}} + 2C_{\text{NEI}}},$$

where C_{NEI} is given by

$$C_{\text{NEI}} = \frac{C_{\text{DEC}} C_{\text{IS}}}{C_{\text{DEC}} + C_{\text{IS}}}.$$

Since we can usually say that $C_{\text{DEC}} \gg C_{\text{IS}}$, we have $K \cong C_{\text{IS}}/C_{\text{DEC}}$.

In DC-coupled detectors, the strips are directly connected to the electronics; the capacitance of a strip towards the input of the amplifier is then given by the Miller capacitance of the preamplifier, that is generally quite higher than the interstrip capacitance. In this case, we can consider $K \cong 0$.

In order to reduce the number of readout channels without spoiling the spatial resolution, intermediate strips can be introduced between two readout strips [17]. In this case charge collected on one intermediate strip is seen by the two neighbouring amplifiers. The ratio of charge seen by the two preamplifiers is linear [13] and given by the ratio of capacitances.

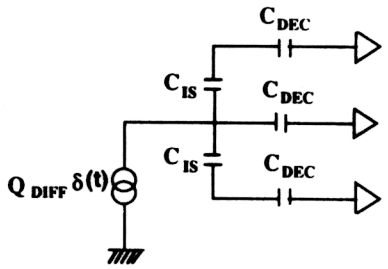

Fig. 1. The detector capacitive network considered in the simulation.

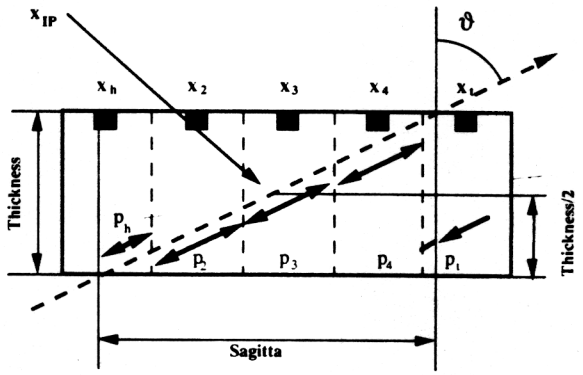

Fig. 2. The geometry considered in the simulation. The impact point x_{IP} is defined as the point where the particle crosses the mid-plane of the detector. The sagitta is the projection of the track along the coordinate measured by the strips. x_i gives the position of the ith strip, while p_i is the length of that part of the track that traverses the volume of the ith strip.

2.1.4. Noise

A random noise sample is added to the charge signal, according to a Gaussian distribution, whose standard deviation is given by the equivalent noise charge (ENC) of the detector–amplifier system.

2.2. Cluster-finding algorithms

Hit search is done using cluster-finding algorithms (CFA), tailored according to the geometry of the tracks [7].

For tracks at 0° or slightly inclined, most of the charge is collected by no more than two strips. For inclined tracks, the charge is spread over several strips. The average number of strips in a cluster is given by geometry (fig. 2) and equal to

$$\langle N_{\text{cluster}} \rangle = \frac{\text{sagitta}}{P} = \frac{t}{P} \tan \vartheta, \qquad (1)$$

where t is the detector thickness and P the readout pitch. The sagitta is defined as the projection on the detector plane of the track in the direction perpendicular to the strips. Apart from the two strips on the edges (what we call the head and the tail), the most probable signal on all the other strips in the cluster is the same and is given by

$$S_\vartheta = \frac{S_0 P}{t \sin \vartheta}, \qquad (2)$$

where S_0 is the most probable signal released by a particle at 0°.

2.2.1. Algorithm for perpendicular or slightly inclined tracks

It is used if the sagitta is smaller than $3P/2$. First a search is done for strips with $(S/N)_{\text{strip}} > 3$, where $(S/N)_{\text{strip}}$ is the signal-to-noise ratio of one strip. Then all the neighbouring strips with positive signals are included in the cluster. This is accepted if: $(S/N)_{\text{cluster}} > S_0/(2 \cos \vartheta \cdot \text{ENC})$, $(S/N)_{\text{cluster}}$ being the sum of $(S/N)_{\text{strip}}$ over all the strips included in the cluster.

2.2.2. Algorithm for inclined tracks

In this case, all the strips with $(S/N)_{\text{strip}} > 3$ are included in the cluster. The search starts from the strip with the highest $(S/N)_{\text{strip}}$ and then moves to the left and to the right, stopping whenever $(S/N)_{\text{strip}}$ falls down the threshold. At this point, the two strips closest to the selected strips are included in the cluster if their signal is positive. The cluster is accepted if $(S/N)_{\text{cluster}} > S_0/(2 \cos \vartheta \cdot \text{ENC})$, and the total number of strips per cluster is higher than half the sagitta (measured in pitch units).

All the events where an accepted cluster has been found are considered as good events and are further analysed. The number of good events divided by the total number of generated events gives the efficiency of the detector.

2.3. One dimensional position-finding algorithm

Several one dimensional position-finding algorithms (PFA), chosen because of their common use and simplicity, have been analysed.

2.3.1. Digital PFA

The position of the cluster is given by the position of the strip with the highest signal. For non-inclined tracks, a simple calculation shows that the standard deviation of the residue distribution generated with this algorithm is

$$\frac{\sigma_{\text{DIG}}}{P} = \frac{1}{\sqrt{12}}.$$

2.3.2. Center-of-gravity (COG) PFA

The position is given by

$$X_{\text{COG}} = \sum_{\text{cluster}} S_i x_i \Big/ \sum_{\text{cluster}} S_i,$$

where x_i is the position of the ith strip included in the cluster and S_i the signal on that strip; the sums are over all the strips included in the cluster. Under given assumptions on noise, it can be shown [18] that the spatial resolution is slightly dependent on the position of the impact point with respect to the collecting electrodes, and, for a given position, it is linearly dependent on the ENC/S ratio. We can consider the impact point position for which the spatial resolution is worst and write

$$\frac{\sigma_{\text{COG}}}{P} \cong a \frac{\text{ENC}}{S}, \tag{3}$$

where a is a coefficient that depends on the hypothesis on noise, as well as on the number of strips included in the cluster. It is equal to 2.12 for 3-strips clusters [18].

2.3.3. Linear PFA

It is the COG PFA applied to two strips. We prefer to analyse it separately from the COG PFA because for small angles ϑ, the signal spreads over at most two strips. The spatial resolution as a function of the impact point x_{IP} is given by

$$\frac{\sigma_{\text{LIN}}}{P} = \frac{\text{ENC}}{S} \sqrt{1 - 2\frac{x_{\text{IP}}}{P} + 2\left(\frac{x_{\text{IP}}}{P}\right)^2}$$

$$= \frac{\text{ENC}}{S} \alpha(x_{\text{IP}}/P). \tag{4}$$

The dependence of the resolution on the impact point is quite smooth, since the function $\alpha(x_{\text{IP}}/P)$ has its minimum for $x_{\text{IP}}/P = 1/2$ where $\alpha = \sqrt{2}/2$ and its maximum at the edge of the definition interval: $\alpha(0) = \alpha(1) = 1$. Eq. (3) still holds with $a = 1$.

2.3.4. Non-linear on η PFA

In the linear PFA, the position is assumed to be given by

$$\frac{x_{\text{LIN}}}{P} = \eta + \frac{x_{\text{L}}}{P},$$

where x_{L} is the position of the left strip in the cluster and the variable η is defined by [19]

$$\eta = \frac{S_{\text{R}}}{S_{\text{R}} + S_{\text{L}}}, \tag{5}$$

where $S_{\text{R(L)}}$ is the signal on the right (left) strip in the cluster.

In the η PFA, the position is assumed to be given by

$$\frac{x_\eta}{P} = f(\eta) + \frac{x_{\text{L}}}{P},$$

where $f(\eta)$ is an arbitrary monotonic growing function of η, with $f(0) = 0$ and $f(1) = 1$. In section 3, this algorithm will be thoroughly analysed because of its importance for tracks at small angles.

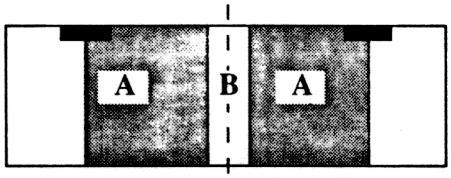

Fig. 3. Definition of regions A and B. The dashed line in region B, represents the border between the two strips. The electric field forces charges on each side of the border to drift towards the closest strip.

2.3.5. Digital head–tail (DHT) PFA

For inclined tracks, a first approach in the calculation of the position consists of considering just the positions, x_h and x_t, of the head and the tail of cluster, respectively (fig. 2)

$$x_{DHT} = \frac{x_h + x_t}{2}.$$

2.3.6. Analog head–tail (AHT) PFA

Since energy loss is roughly proportional to the particle path in silicon, an AHT PFA can be defined in the following way (fig. 2):

$$\frac{x_{AHT,0}}{P} = \frac{x_{DHT}}{P} + \frac{S_h - S_t}{2S_\vartheta}. \tag{6}$$

In order to reduce the influence of Landau fluctuations, we can further refine the definition of the AHT by writing

$$\frac{x_{AHT}}{P} = \frac{x_{DHT}}{P} + \frac{\min(S_h, S_\vartheta) - \min(S_t, S_\vartheta)}{2S_\vartheta}. \tag{7}$$

Experimental results [7] as well as our Monte Carlo simulations show that the AHT defined with eq. (7) gives slightly better results than the one defined by eq. (6). In the following, unless otherwise specified, we will suppose the AHT defined with eq. (7).

2.3.7. One-sided analog head–tail (1S-AHT) PFA

The algorithms presented in 2.3.5 and 2.3.6 demand the knowledge of both the head and the tail of the cluster. However, if we know the angle of the track, the position and pulse-height of one of the two edges is sufficient to find the position of the cluster. For example, using the head (left edge) of the cluster we can say that the position of the impact point is given by

$$\frac{x_{AHT,h}}{P} = \frac{x_h}{P} + \frac{1}{2} - \frac{S_h}{S_\vartheta} + \frac{t \tan \vartheta}{2P}. \tag{8}$$

A similar definition applies for the tail strip.

3. The η algorithm

3.1. The η variable and its distribution

Before considering the effect of the η PFA on the spatial resolution, we will first consider the distribution of the variable η and its physical origin.

Many experimental results are currently available about this fundamental distribution in microstrip detectors [6,7,19,20]. A common feature of all the experimental results is the presence of peaks in the η distribution. This means that charge division is far from being linear, because, if this was the case, the η distribution should be flat. This observed non-linearity can be fully explained by the width of the diffusion cloud.

For perpendicular tracks, charge spread is dominated by diffusion. The width of the charge cloud depends on detector parameters as the thickness, the resistivity and the applied voltage. For most of the detectors used in high-energy physics, the thickness is around 300 μm and the resistivity is a few kΩ cm; this gives a width of the diffusion cloud of about 5–10 μm for a fully depleted detector. Thus, the charge cloud is far smaller than the pitch in most of the microstrip detectors in use.

How can we see this effect in the experimental data? Let us consider a detector where every strip is read out. If a particle hits the detector in the middle between two strips (region B in fig. 3), charge division will be effective (and roughly linear). On the contrary, if the particle crosses the detector about 10 μm away from the strip frontier (region A in fig. 3), most of the charge will flow to one strip. In this region, η will assume a value close to 0 or 1. The width of region B, where charge division is effective, depends only on diffusion, thus the width of region A is larger for larger pitches. For example, in a 50 μm pitch detector, region A and B have roughly the same width. Since in region B, η spans over a large set of values while in A it is confined in a small region around the edges, the η distribution will have peaks close to the value $\eta = 0$ and $\eta = 1$.

If an intermediate strip is introduced, the peaks at $\eta \approx 0$ and $\eta \approx 1$ will still be there, but a new peak at $\eta = 1/2$ will appear, corresponding to the intermediate strip (see fig. 6). The three peaks will also be less pronounced than in the previous case, since the strip pitch gets closer to the width of the diffusion cloud.

Diffusion alone can thus explain the main feature of the η distribution, i.e. its non-linearity, but cannot explain all its characteristics. Let us again consider a 50 μm pitch detector, where every strip is read out. If the capacitive coupling and the noise are switched off, two very narrow peaks at $\eta = 0$ and $\eta = 1$ appear (fig. 4). If we now introduce the capacitive coupling (fig. 4), the

two peaks move to the center by an equal quantity $K/(1-K) \approx K$, because some fraction of the charge always flows to neighbouring strips.

Now noise is switched on. The two peaks spread out, and their width is determined by the noise magnitude. Since η can be considered as the signal on one strip normalized to the total signal in the cluster, the width of the two peaks is roughly given by

$$\sigma_{\text{peak}} \approx \frac{\text{ENC}}{S} = \frac{1}{S/N}. \tag{9}$$

This equation is confirmed by experimental results (fig. 5) as well as by the simulation.

3.2. The η algorithm

Since hits are uniformly distributed over the detector, the position of the cluster with respect to the left strip can be calculated with:

$$x_\eta = P\frac{\int_0^{\eta_0} \frac{dN}{d\eta} d\eta}{\int_0^1 \frac{dN}{d\eta} d\eta} = Pf(\eta_0), \tag{10}$$

where $dN/d\eta$ gives the differential η distribution. Eq. (10) defines a non-linear algorithm (see section 2.3.4) with $f(\eta)$ given by the integral of the η distribution, normalized to the total number of events in the distribution.

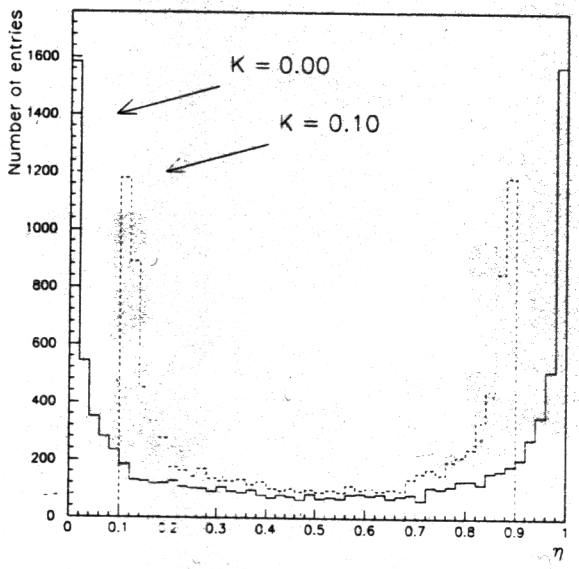

Fig. 4. The distribution of the variable η obtained with the Monte Carlo simulation in the absence of noise and for two different values of the capacitive coupling K ($P = 50$ μm and no intermediate strip).

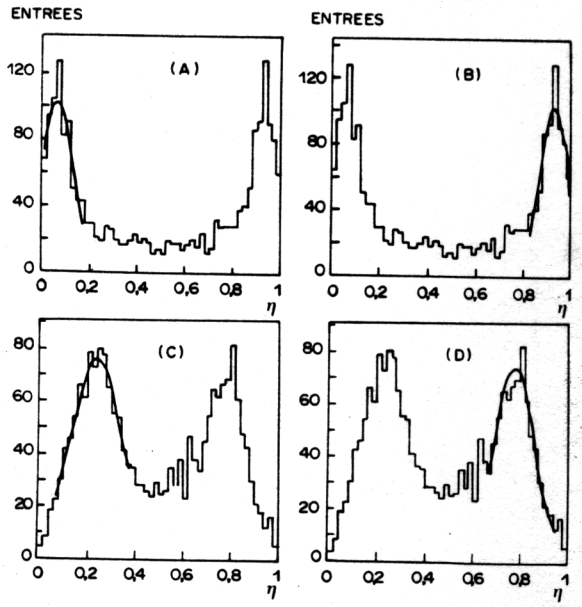

Fig. 5. The experimental distributions of the variable η with a Gaussian fit on the peaks for two different values of the S/N in a 50 μm pitch detector without any intermediate strip. (a) and (b) $S/N = 16$; (c) and (d); $S/N = 10$. The inverse of the standard deviation of the Gaussian fits are 15.2 and 16.5 in (a) and (b) respectively, and 9.3 and 11.2 in (c) and (d) respectively.

A comparison between the plot of the true impact point as a function of η [6] and the function $f(\eta)$ shows this algorithm correctly reconstructs the impact point position. On the contrary, a linear algorithm generates systematic errors.

We remark that the η algorithm uses only intrinsic properties of the detector in order to correct for its non-linearities.

3.3. Spatial resolution in the case of non-linear charge division

Eq. (4) gives the spatial resolution that can be expected when using the linear PFA, under the hypothesis that *this algorithm correctly reconstructs the position in the absence of noise.* But, as we saw in the previous section, this is not the case in microstrip detectors for tracks at 0° (or slightly inclined, so that diffusion is still the dominant factor in the charge division). In this case, the η PFA gives the correct position. Using eq. (10) and error propagation, we can write

$$\sigma_{x_\eta}^2 = P^2\left(\frac{df}{d\eta}\right)^2 \sigma_\eta^2.$$

The error σ_η on the determination of η can be easily obtained from eq. (4), observing that in the linear algorithm $x/P = \eta$. Thus,

$$\sigma_\eta = \frac{\mathrm{ENC}}{S}\sqrt{1-2\eta+2\eta^2}$$

and, from eq. (10),

$$\frac{\mathrm{d}f}{\mathrm{d}\eta} = \frac{\dfrac{\mathrm{d}N}{\mathrm{d}\eta}}{\displaystyle\int_0^1 \frac{\mathrm{d}N}{\mathrm{d}\eta}\mathrm{d}\eta},$$

that is $\mathrm{d}f/\mathrm{d}\eta$ is given by the number of entries in the η distribution normalized to the total number of entries N_{tot}. The spatial resolution obtained with the η algorithm is then given by

$$\frac{\sigma_{x_\eta}}{P} = \frac{\mathrm{ENC}}{S}\sqrt{1-2\eta+2\eta^2}\,\frac{\dfrac{\mathrm{d}N}{\mathrm{d}\eta}}{\displaystyle\int_0^1 \frac{\mathrm{d}N}{\mathrm{d}\eta}\mathrm{d}\eta}$$

$$= \frac{\mathrm{ENC}}{S}\alpha(\eta)\frac{1}{N_{\mathrm{tot}}}\frac{\mathrm{d}N}{\mathrm{d}\eta}, \qquad (11)$$

where $\eta = f^{-1}(x/P)$.

As we described in section 2.3.3, the function $\alpha(\eta)$ is quite flat, ranging from $\sqrt{2}/2$ up to 1. On the contrary, the distribution of η is far from being flat. The term $\mathrm{d}N/\mathrm{d}\eta$ in eq. (11) gives then rise to dramatic non-uniformities in the spatial resolution. We can define a resolution function $R(x)$ such that

$$\frac{\sigma_{x_\eta}}{P} = \frac{\mathrm{ENC}}{S}R(x). \qquad (12)$$

Microstrip detectors have thus a highly non-uniform spatial resolution, as already observed in ref. [6], and residue distribution is far from being Gaussian. The FWHM of the residue distribution reflects the response of region B, where spatial resolution has its optimum, while a Gaussian fit represents, in some sense, an average of the detector spatial resolution.

We can ask ourselves the question: what is the function f that gives the best resolution? It is easy to show (see appendix A) that at equal signal-to-noise ratio the best resolution is obtained for the function $f(\eta) = \eta$, that is in the case of linear charge division.

3.4. How to get a linear charge division

It is thus important to get a charge division as linear as possible. In section 3.1, we showed non-linearities arise because of the shape of the diffusion cloud. If σ_{diff} is the standard deviation of this cloud, non-linearities are large if the ratio P/σ_{diff} is large. We need then to reduce this ratio.

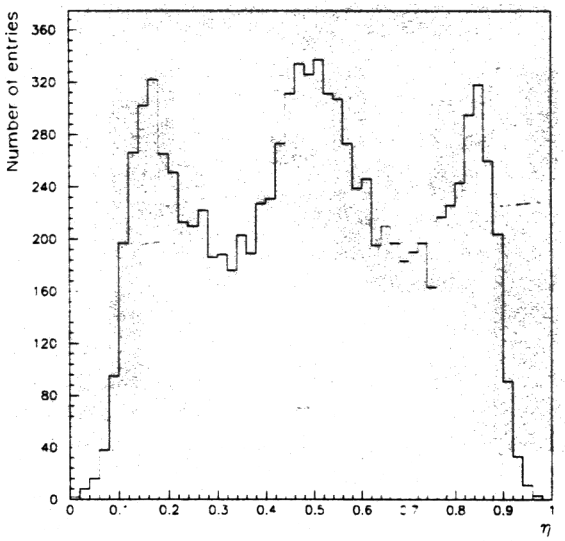

Fig. 6. The simulated distribution of the variable η for a detector with one intermediate strip, $P = 50$ μm and $S/N = 20$.

The first way is to increase σ_{diff}. This can be done by thickening the detector and applying the minimum biasing voltage capable of fully depleting the detector. This is not always possible because other considerations, such as a minimum amount of matter, in order to reduce multiple scattering, set a limit to the thickness of the detector. Moreover, a thicker detector suffers from a higher probability of δ-rays production. δ-rays

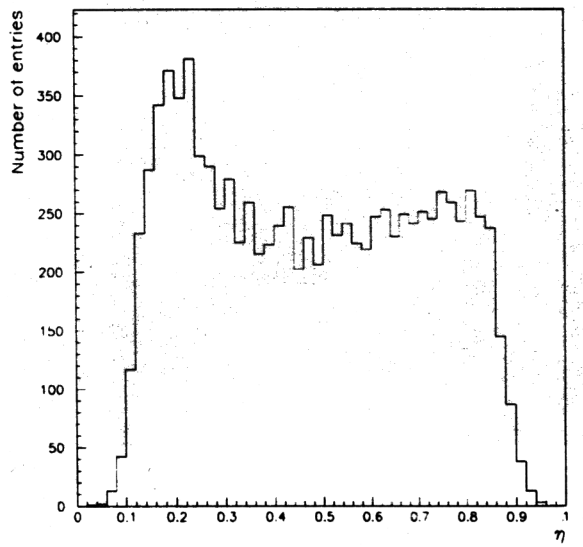

Fig. 7. The simulated distribution of the variable η for a detector with no intermediate strip, $P = 50$ μm, $S/N = 20$ at an angle $\vartheta = 10°$. The asymmetry in the η distribution is due to the geometry.

can displace the centroide of the charge cloud and limit the spatial resolution [21].

We are thus left with the second possibility, i.e. reducing P. This can be done without increasing the number of electronic readout channels by introducing an intermediate strip between two readout strips for charge interpolation. The resulting η distribution (fig. 6) is less peaked and charge division is almost linear.

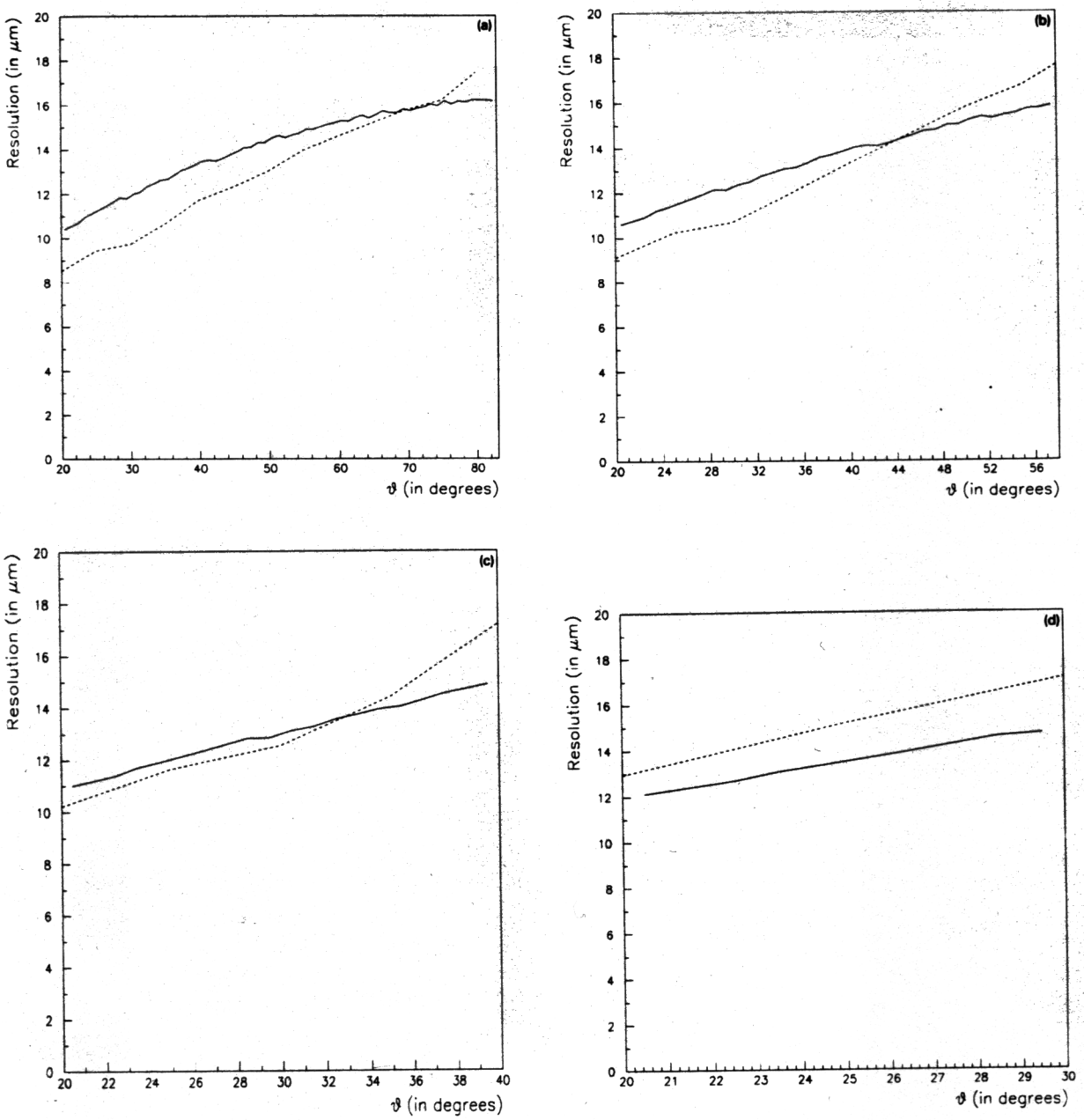

Fig. 8. Comparison of Monte Carlo calculation of the spatial resolution (dashed line) and of the values given by eq. (18). The function $\pi(p)$ has been calculated using the analytic expressions for the most probable value and the FWHM of the energy loss distribution given on page 648 in ref. [22]. For each angle, eq. (18) has been calculated for the different positions of the impact point and then an average value has been calculated. In the figure the comparison is done for a 50 μm pitch detector, assuming $C = 1$. Similar agreement is obtained for different pitches. The curves are given only in the angular range between ϑ_{min} and ϑ_{max} where eq. (18) applies. (a) $S/N = 25$; (b) $S/N = 20$; (c) $S/N = 15$; (d) $S/N = 10$.

3.5. Slightly inclined tracks

In this paragraph we consider angles ϑ small enough so that most of the charge is collected by two strips. The η distribution becomes less and less peaked for increasing angle (fig. 7), that is charge division becomes more and more linear. We thus expect to find a minimum for the spatial resolution for the angle ϑ such that

sagitta ≈ 1

or

$$\vartheta_{opt} \approx \tan^{-1}\left(\frac{P}{t}\right). \tag{13}$$

At $\vartheta = \vartheta_{opt}$ the charge division is almost linear and thus spatial resolution can be roughly calculated with eq. (3), with $a = 1$.

4. The analog head–tail algorithms

4.1. Analog head–tail. Spatial resolution

In this paragraph we present an approximate calculation of the spatial resolution obtained with the AHT PFA. In order to simplify the calculation, we consider expression (6) instead of (7).

We define $S_h(S_t)$ as the most probable energy loss on the head (tail) strip corresponding to the path of the particle in the detector. We can write for the true impact point (see fig. 2)

$$\frac{x_{IP}}{P} = \frac{x_h + x_t}{2} + \frac{S_t - S_h}{2S_0}\frac{t \sin\vartheta}{P}. \tag{14}$$

If we consider to be able to correctly reconstruct the cluster, the measured position will be given by

$$\frac{x_{MEAS}}{P} = \frac{x_h + x_t}{2} + \frac{S_t + N_t - S_h - N_h}{2S_0}\frac{t \sin\vartheta}{P}, \tag{15}$$

where N_h and N_t express the deviation of the measured pulse-height from the most probable value. The error on the measurement of the position is then given by:

$$\frac{\Delta x}{P} = \frac{N_t - N_h}{2S_0}\frac{t \sin\vartheta}{P}$$

and the spatial resolution is given by the standard deviation of this quantity. The deviations N_h and N_t are generated by two noise sources: i) Landau fluctuations; ii) electronic noise. We can suppose these two sources are uncorrelated, and write, for an arbitrary strip

$$\langle N^2 \rangle = \langle N^2_{Landau} \rangle + \langle N^2_{Electronics} \rangle.$$

The second term is easily evaluated and given by

$$\langle N^2_{Electronics} \rangle = \mathrm{ENC}^2. \tag{16}$$

The first one cannot be calculated in an analytic fashion, so we need some approximate expression. The dispersion of values around the most probable one S_p is usually described by the FWHM w_p of the distribution. The ratio $\pi(p) = w_p/S_p$ is not constant, but tends to increase for decreasing path length p, and it ranges from about 1 for a pathlength of a few microns to about 0.4 for $p \approx 300$ μm [22]. We can then write

$$\langle N^2_{Landau} \rangle = \left[\pi(p) S_p \frac{1}{C}\right]^2, \tag{17}$$

where C is a coefficient that gives the ratio between the full width at half-maximum and the standard deviation of the distribution, and it is equal to 2.36 in the case of a Gaussian distribution. For the energy loss distribution, no simple analytical expression of its standard deviation exists so that we can just rely on approximations. The results obtained in this paragraph are in good agreement with those of the simulation for $C = 1$ (fig. 8).

Using eqs. (16) and (17), and assuming N_t and N_h are uncorrelated, the standard deviation of the error on the position measurement is thus given by:

$$\begin{aligned}\frac{\Delta x^2}{P^2} &= \left\{2\,\mathrm{ENC}^2 + \left[\pi(p_h) p_h S_\vartheta / p_0 C\right]^2 \right.\\ &\quad \left. + \left[\pi(p_t) p_t S_\vartheta / p_0 C\right]^2\right\}/(2S_\vartheta)^2\\ &= \left(\frac{1}{2}\right)^2 \left\{2\left(\frac{\mathrm{ENC}}{S_0}\frac{t \sin\vartheta}{P}\right)^2 \right.\\ &\quad \left. + \frac{\left[\pi(p_h) p_h / p_0\right]^2 + \left[\pi(p_t) p_t / p_0\right]^2}{C^2}\right\}, \end{aligned} \tag{18}$$

where $S_h = p_h S_\vartheta / p_0$ and $p_0 = P/\sin\vartheta$.

In this formula we recognize two terms. The first one is due to the electronic noise: it is inversely proportional to the signal-to-noise ratio (measured at 0°), and depends on a geometric factor $t \sin(\vartheta)/P = S_0/S_\vartheta$ that takes into account the reduction of the strip signal with the angle.

The second term in eq. (18) is due to Landau fluctuations. We observe that this term is dependent on the impact point position in a complicated way, through the function $\pi(p)$ and p_h and p_t. We will not analyse this dependence since it does not give rise to any large non-uniformity in the spatial resolution as we described in section 3. Since, on the average, the length of the path in the volume of one strip decreases with the angle, and that $\pi(p)$ is a decreasing function of the path, the total average effect is that the second contribution to eq. (18) also increases with the angle.

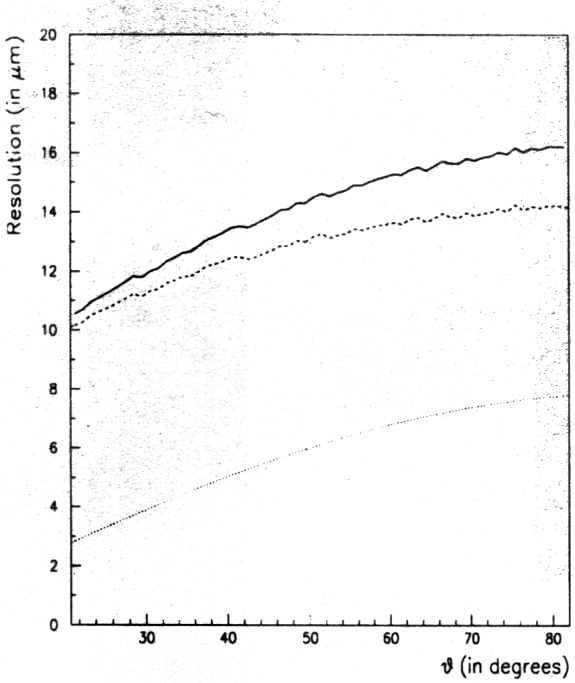

Fig. 9. The relative contributions of electronic noise (dotted line) and Landau fluctuations (dashed line) are compared to the spatial resolution for a 50 μm pitch detector with no intermediate strip and $S/N = 25$. The curves are given only in the angular range between ϑ_{min} and ϑ_{max} where eq. (18) applies. Similar curves are obtained for different detector designs.

Before discussing the range of application of eq. (18), we will compare the relative importance of the two terms appearing there. We suppose $P = 100$ μm and $S_0/\mathrm{ENC} = 15$. We also suppose that $\pi(p_h) = \pi(p_t) = 0.6$ and $p_h/p_0 = p_t/p_0 = 0.5$; taking $C = 1$, the second term is equal to 0.180, while the first one is given by $0.045\ (\sin\vartheta)^2$, that is the error on the determination of the position is dominated by Landau fluctuations (fig. 9).

Eq. (18) cannot be applied on the whole range of ϑ. First of all, we supposed that eq. (14) gives the correct impact point. This is true when the sagitta is larger than 2P. Using eq. (1), the minimum angle for which we can apply eq. (18) is then given by

$$\vartheta_{min} \approx \tan^{-1}\left(\frac{2P}{t}\right). \tag{19}$$

This angle depends only on the ratio P/t, being larger for larger pitch. For $P = 50$ μm, $\vartheta_{min} \approx 18°$, and for $P = 200$ μm, $\vartheta_{min} \approx 55°$.

In order to determine the maximum angle for which eq. (18) can be used, we remark that we supposed that the cluster has been correctly defined, that is the head and the tail of the cluster are correctly identified and that any error on the measured position comes from electronic noise and Landau fluctuations on those strips. As a matter of fact, another possible source of error is an incorrect reconstruction of the cluster. With the CFA presented in section 2.2.2, this happens whenever the signal on one of the *internal* strips in the cluster (that is the strips that are neither the head nor the tail) is lower than the threshold. If this happens the reconstructed cluster will contain less strips than expected and the reconstructed position will be displaced by some amount. Since the most probable signal on the internal strips is given by eq. (2), we can suppose the cluster will be correctly reconstructed if

$$S_\vartheta = \frac{S_0 P}{t \sin\vartheta} > \text{constant} * \mathrm{ENC}$$

A reasonable choice of the constant is 4. This gives for the maximum angle the following expression

$$\vartheta_{max} \approx \sin^{-1}\left(\frac{1}{4}\frac{S_0}{\mathrm{ENC}}\frac{P}{t}\right) \tag{20}$$

and thus it depends on S/N as well as on the ratio P/t.

4.2. 1-sided analog head–tail. Spatial resolution

In the same way as we did in the previous paragraph, we can calculate the spatial resolution in the case of the 1S-AHT PFA. The error on the position is now given by

$$\frac{\Delta x}{P} = \frac{N_t}{S_0}\frac{t \sin\vartheta}{P}$$

and its variance is

$$\frac{\Delta x^2}{P^2} = \left(\frac{\mathrm{ENC}}{S_0}\right)^2\left(\frac{t \sin\vartheta}{P}\right)^2 + \frac{\left[\pi(p_t)p_t/p_0\right]^2}{C^2}. \tag{21}$$

A comparison of formulae (18) and (21) shows that the spatial resolution of the 1S-AHT PFA is roughly that of the AHT PFA times $\sqrt{2}$, that is usually the 1S-AHT algorithm performs worse than the AHT PFA. However, at very large angles, that is for angles of the order of ϑ_{max} or larger, the simulation shows that the 1S-AHT PFA gives better results than the AHT PFA. This effect can be explained as follows: in this angular range the $(S/N)_{strip}$ is poor, so that it is quite difficult to correctly reconstruct the clusters. A wrong reconstruction happens whenever the $(S/N)_{strip}$ of one of the internal strips drops below the selected threshold. The loss of only one of the internal strips is sufficient to cause a wrong determination of one of the two edge strips. In this case, the AHT PFA will always give a wrong value of the cluster position, while each of the two 1S-AHT algorithms will correctly calculate the cluster position in half of the cases. Thus the 1S-AHT algorithms give better results than the AHT PFA at

very large angles. However, we must be aware of the fact that in this angular range, the efficiency of the detector is sensibly less than 100% (see fig. 13), so that we should avoid operating in this region.

5. Simulation results and comparison with experiments

5.1. Simulation results

Before considering the simulation results, we will summarize the analysis of sections 3 and 4.

At small angles, the charge division is non-linear, mainly due to diffusion. The non-linear algorithm based on the differential distribution of the η variable allows a correction of this non-linearity. It should thus give the best results among all the considered algorithms. Since it is based on the pulse-height of the two adjacent strips that collect most of the charge, it loses its effectiveness when the charge spreads over more than two strips. This constraint sets an upper limit to the angular range where the η algorithm should be applied, and this upper limit can be determined by setting sagitta ≤ 1, that is the upper limit is equal to ϑ_{opt} (see section 3.5). The spatial resolution obtained with the η algorithm improves when increasing ϑ from 0° to ϑ_{opt}, because the charge division becomes increasingly linear.

At large angles, the charge spreads over several strips but the information on the cluster position is contained only in the position and the pulse-height of the two edge strips, the head and the tail of the cluster. The AHT algorithm exploits this property of the clusters and should thus give the best resolution at large angles. As we discuss in section 4, the AHT is effective in the angular range $\vartheta_{min} < \vartheta < \vartheta_{max}$. Beyond this upper limit the $(S/N)_{strip}$ becomes so poor that it is very difficult to correctly reconstruct the cluster, and then the two edge strips. For $\vartheta > \vartheta_{max}$, we expect the 1S-AHT to give better results, even though we should be aware that at these very large angles the efficiency of the detector is poor.

Our analysis shows what is the best algorithm to be used for the whole angular range, expect for the interval $\vartheta_{opt} < \vartheta < \vartheta_{min}$. Before considering the results of the simulation, we can try to find the best algorithm in this range with some simple considerations. For $\vartheta \approx \vartheta_{opt}$, the charge division is almost linear and most of the signal is collected by two strips so that the η algorithm computes the same cluster position as the COG PFA. For $\vartheta \approx \vartheta_{min}$, most of the charge is spread over three strips and we can find that in this case the COG PFA gives roughly the same cluster position as the AHT does (see appendix B). Thus, the COG PFA represents a sort of compromise between the η and the AHT algorithms and we can expect the COG PFA to give the best results in the angular region under consideration.

Our expectation about the best algorithm are summarized in table 1. They are confirmed by the simulation (fig. 10).

We have simulated 300 μm thick detectors with several values of the readout pitch and of S/N, and

Table 1
The algorithm that gives the best spatial resolution as a function of the track angle ϑ

Angular range		Best algorithm
Small angles:	$0 < \vartheta < \vartheta_{opt}$	η
Intermediate angles:	$\vartheta_{opt} < \vartheta < \vartheta_{min}$	COG
Large angles:	$\vartheta_{min} < \vartheta < \vartheta_{max}$	AHT
Very large angles:	$\vartheta > \vartheta_{max}$	1S-AHT (but poor efficiency)

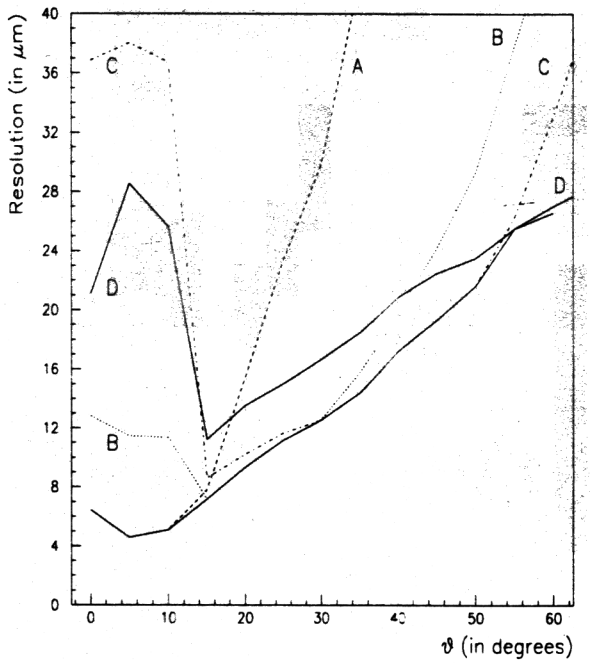

Fig. 10. The spatial resolution as a function of ϑ is shown for different algorithms together with the best results. The simulated detector has $P = 50$ μm, $S/N = 15$ and no intermediate strip. A similar behaviour is obtained for different configurations. The lowest curve is the resolution measured taking the best algorithm at each angle. The other four curves give the resolution measured with: (A) the η algorithm (dashed line); (B) the center-of-gravity algorithm (dotted line); (C) the analog head–tail algorithm (dash-dotted line); (D) the one-sided analog head–tail algorithm (upper full line). At 60°, the best results are obtained by using the other one-sided analog head-tail algorithms (the two 1S-AHT give almost equal but not identical values for the resolution).

with zero or one intermediate strips. The simulation was done for angles ϑ ranging from 0 to 80° with a 5° step. Figs. 11 and 12 show the spatial resolution, obtained with a Gaussian fit to the residue distribution. At each angle, we considered the result of the algorithm that gives the best spatial resolution. In fig. 13

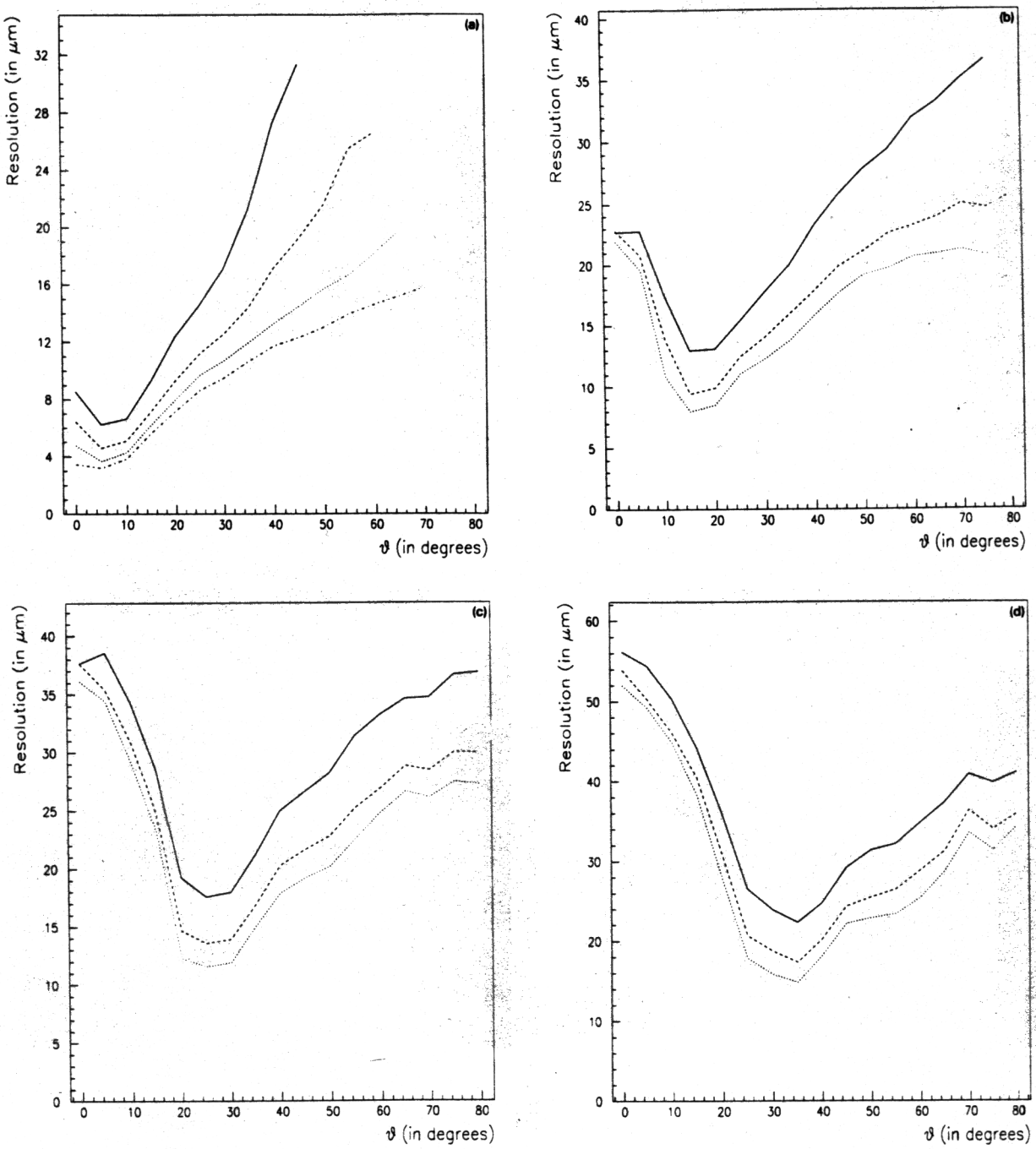

Fig. 11. Spatial resolution as a function of ϑ. No intermediate strip. The curve are drawn up to ϑ_{max}. (a) Detector with a 50 μm readout pitch. The considered S/N are 25, 20, 15, 10, the lowest curve corresponding to the highest signal-to-noise ratio. (b) Detector with a 100 μm readout pitch. S/N = 20, 15 and 10. (c) Detector with a 150 μm readout pitch. S/N = 20, 15 and 10. (d) Detector with a 200 μm readout pitch. S/N = 20, 15 and 10.

the efficiency is shown for detectors with no intermediate strips and a pitch of 50 and 100 μm.

Let us first consider the curves for detectors with no intermediate strips (fig. 11). Some common features can be observed. The spatial resolution improves when going from 0° to ϑ_{opt}, goes through a minimum at ϑ_{opt} and then worsens steadily. The position of the minimum depends only on the pitch and not on the signal-

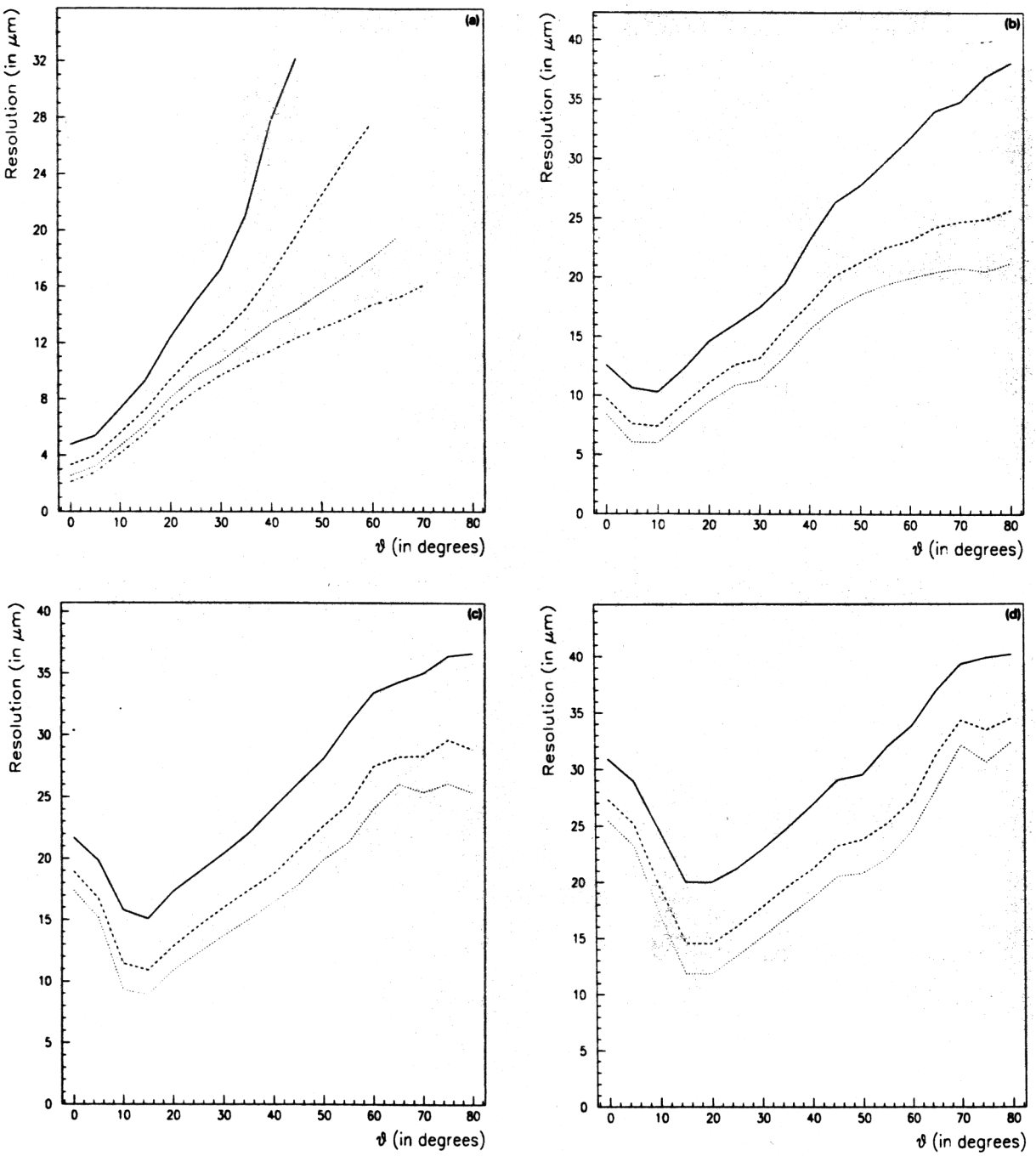

Fig. 12. Spatial resolution as a function of ϑ. One intermediate strip. The curves are drawn up to an angle ϑ_{max}. (a) Detector with a 50 μm readout pitch. The considered S/N are 25, 20, 15, 10, the lowest curve corresponding to the highest signal-to-noise ratio. (b) Detector with a 100 μm readout pitch. S/N = 20, 15 and 10. (c) Detector with a 150 μm readout pitch. S/N = 20, 15 and 10. (d) Detector with a 200 μm readout pitch. S/N = 20, 15 and 10.

to-noise ratio (see section 3.5). At equal S/N, we get the best spatial resolution with the smallest pitch, but the differences are less large for large angle. For example, if we consider the curves for $S/N = 20$, at $\vartheta = 5°$ the spatial resolution for $P = 50$ μm is slightly better than 4 μm while for $P = 100$ μm it is about 20 μm. At $\vartheta = 15°$, where the curve for $P = 100$ μm reaches its minimum, the spatial resolutions are 6.2 and a 7.9 μm respectively, and for $\vartheta = 60°$, they are about 18 and 20 μm respectively. Moreover (see fig. 13), at $\vartheta = 60°$, the efficiency of the 50 μm pitch detector has already dropped to 95% while that of the 100 μm pitch detector is still 100%.

We can now consider the curves in fig. 12, obtained for the same detector configurations as those of fig. 11, but with the addition of one intermediate strip. At small angles, this strip improves the resolution of the detector because it makes the charge division more linear. For $P = 50$ μm, the charge division is already almost linear at 0°, and the spatial resolution is at its optimum. For the other pitch values, the curves of fig. 12 show minima, whose positions are shifted towards smaller angle with respect to the minima in the curves of fig. 11. An analysis of these curves shows that the position of the minimum can be still given by eq. (13), but where P is taken as the strip pitch, that is half the readout pitch. At large angle, the charge division is mainly determined by Landau fluctuations and not by diffusion, so that the intermediate strip does not play any role, and, for $\vartheta > \vartheta_{min}$, we obtain the same spatial resolution with or without any intermediate strip.

We must stress the fact that at equal strip pitch, but different readout pitch, we get the best resolution with the smallest readout pitch over the full angular range. This can be seen by comparing, for example, figs. 11b and 12d, obtained for detectors with the same strip pitch (100 μm), but with different readout pitches (100 and 200 μm, respectively).

5.2. Simulation versus experiments

Up to now only a few measurements of spatial resolution versus track angle are available. Moreover, our analysis has shown that different algorithms give different values of the spatial resolution, so that a direct comparison is possible only for those measurements which employ the same position-finding algorithm.

In ref. [7] the algorithms presented in this paper were used in the analysis of the experimental data. The experimental curve obtained for a detector with 50 μm readout as well as strip pitch and a $S/N \approx 27$ is drawn in fig. 14 (black circles) together with the simulated values (triangles). In the region between 0 and 10°, the experimental resolution is constant within the experimental error, even though a minimum seems to appear

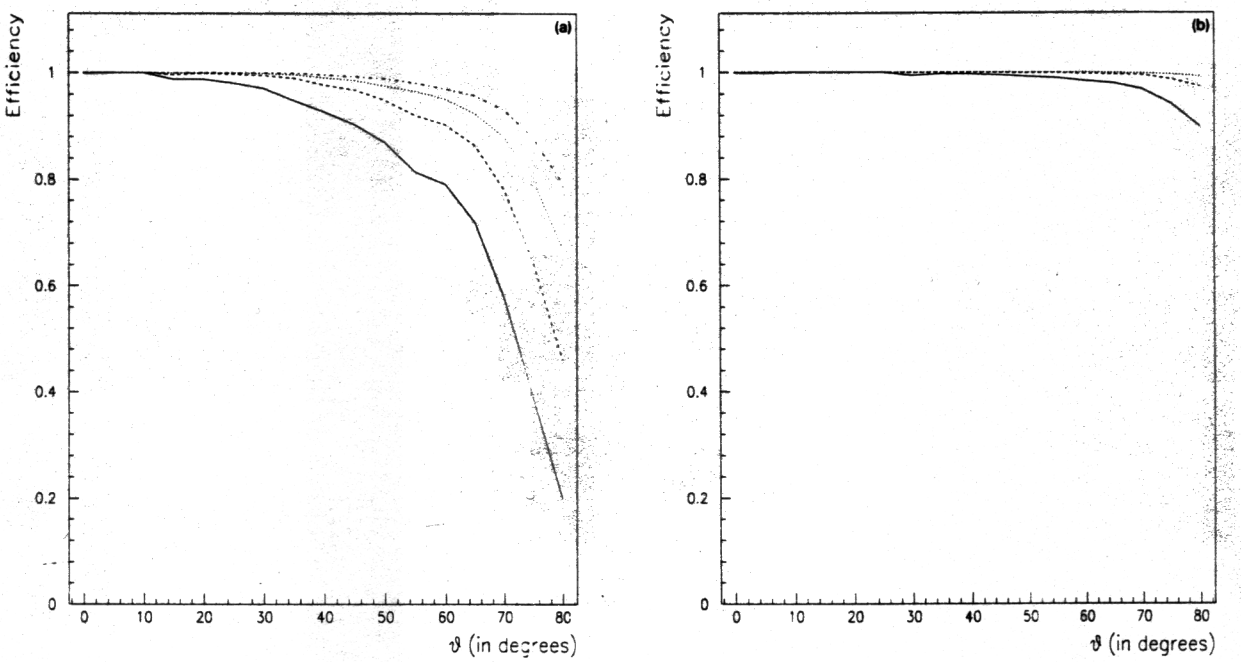

Fig. 13. Efficiency as a function of ϑ. No intermediate strip. (a) Detector with a 50 μm readout pitch. The considered S/N are 25, 20, 15, 10, the lowest curve corresponding to the lowest signal-to-noise ratio. (b) Detector with a 100 μm readout pitch. $S/N = 20$, 15 and 10.

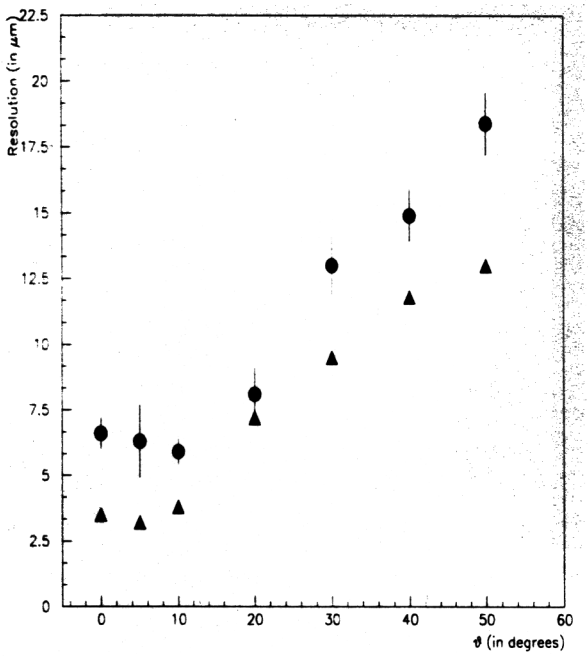

Fig. 14. Comparison between simulation (triangles) and experimental data (circles).

between 5 and 10°. This agrees with the simulated results where a slightly pronounced minimum is found at $\vartheta = 5°$. For angles larger than 10°, both simulation and experiments show a constant decrease in resolution. The simulation results are systematically better than the experimental ones, and this is probably due to the fact that the simulated conditions are ideal (no noisy or dead strip, ideal alignment, etc.).

Our simulation well reproduces the trend of experimental data in this case and we hope that in the near future more experimental data will become available for comparison.

6. Conclusions

Our analysis shows the importance of the choice of the position-finding algorithm in the optimisation of the spatial resolution of a microstrip detector. From the point of view of the choice of the best algorithms, four angular domains can be distinguished. At small angle, where diffusion is important, the η algorithm, that takes into account non-linearities in charge division, gives the best performances. At large angle, a simple linear (the analog head-tail) algorithm that uses only the signal of the two edge strips in the cluster gives the best results. In the intermediate region between the domains of small and large angles, the well-known center-of-gravity algorithm represents a compromise between the η and the AHT algorithms and gives the best results. For very large angles, where the detector efficiency is substantially lower than 100%, a simplified version of the AHT PFA, the one-sided analog head–tail algorithm, has demonstrated best performances.

In terms of detector design, for small angle it is clear that at equal S/N the pitch should be kept as small as possible in order to optimise the spatial resolution. At large angle this is still true, but a compromise must be found between good spatial resolution and high efficiency. Eventually, the requirement of high efficiency sets a limit on the pitch and, thus, on the spatial resolution.

The algorithms presented here have been developed and analysed in the case of microstrip detectors, but they can be applied to any segmented silicon detector. For example, the non-linear algorithm has already been successfully applied to silicon pixel detectors [23]. The algorithms for inclined tracks could also be used, thus giving a first approach towards the optimum algorithm in pixel detectors.

Appendix A: Determination of the function $R(x)$

We suppose that the spatial resolution σ_{DET} is obtained by averaging over the spatial resolution as a function of the impact point, i.e.

$$\left(\frac{\sigma_{\mathrm{DET}}}{P}\right)^2 = \left(\frac{1}{P}\right)^2 \int_0^P [\sigma(x)]^2 \, \mathrm{d}x.$$

In the case we are considering it is

$$\left(\frac{\sigma_{\mathrm{DET}}}{P}\right)^2 = \left(\frac{\mathrm{ENC}}{S}\right)^2 \int_0^1 [R(x)]^2 \, \mathrm{d}x$$

and we want to determine the function $R(x)$ for which the integral is minimum.

We express the resolution function as the sum of two terms:

$$R(x) = 1 + g'(x),$$

where $g'(x)$ is the derivative of an arbitrary function g, with the condition that

$$g(0) = g(1).$$

This condition is not restrictive at all, because the function f is usually symmetric with respect to $1/2$.

We thus have

$$\int_0^1 [R(x)]^2 \, \mathrm{d}x = \int_0^1 [1 + g'(x)]^2 \, \mathrm{d}x$$

$$= 1 + 2\int_0^1 g'(x) \, \mathrm{d}x + \int_0^1 [g'(x)]^2 \, \mathrm{d}x$$

$$= 1 + \int_0^1 [g'(x)]^2 \, \mathrm{d}x \geq 1,$$

where the equality holds only in the case where $R(x) \equiv 1$.

In the case we are considering

$$R(x) = \left\{ \alpha(\eta) \frac{1}{N_{\text{tot}}} \frac{\mathrm{d}N}{\mathrm{d}\eta} \right\}_{\eta = f^{-1}(x/P)}.$$

Since $\alpha(\eta)$ is flat and quite close to 1, we must have $\mathrm{d}N/\mathrm{d}\eta$ = constant.

Appendix B. The center-of-gravity (COG) algorithm at $\vartheta \approx \vartheta_{\text{min}}$

We consider the situation $\vartheta = \vartheta_{\text{min}}$. In this case (see eq. (19)) the sagitta is equal to 2 (in pitch units) and we can consider that the signal spreads over three strips, strip 0, 1 and 2. The cluster position calculated with the COG PFA is

$$\frac{x_{\text{COG}}}{P} = \frac{x_0 S_0 + x_1 S_1 + x_2 S_2}{S_0 + S_1 + S_2} = \frac{S_1 + 2S_2}{S_0 + S_1 + S_2},$$

while that measured by the AHT PFA is

$$\frac{x_{\text{AHT}}}{P} = \frac{x_0 + x_2}{2} + \frac{S_2 - S_0}{2S_\vartheta} = 1 + \frac{S_2 - S_0}{2S_\vartheta},$$

where S_i is the pulse-height measured on the ith strip.

We can say that for the internal strip (strip no. 1) we have $S_1 \approx S_\vartheta$, while for the total charge $S_0 + S_1 + S_2 \approx 2S_\vartheta$. Thus

$$\frac{x_{\text{COG}}}{P} = \frac{S_1 + 2S_2}{S_0 + S_1 + S_2} = \frac{S_0 + S_1 + S_2 + S_2 - S_0}{S_0 + S_1 + S_2}$$

$$= 1 + \frac{S_2 - S_0}{S_0 + S_1 + S_2} \approx 1 + \frac{S_2 - S_0}{2S_\vartheta} = \frac{x_{\text{AHT}}}{P},$$

that is the COG and the AHT calculate roughly the same cluster position.

Acknowledgements

Many fruitful discussions with Peter Weilhammer, CERN, are at the origin of this work. Prof. M. Schaeffer, LEPSI, has always warmly supported and encouraged this work. I also wish to acknowledge M. Tyndel, RAL, project leader of the DELPHI Microvertex Upgrade, for the kind permission of using the experimental data taken in the DELPHI beam test. D. Husson, LEPSI, and R. Roy, LGME Strasbourg, carefully read and commented the draft of this paper.

References

[1] P. Weilhammer, CERN-EP/86-54, presented at the workshop on New Solid State Devices for High-Energy Physics, Berkeley, October 28–30, 1985.
[2] N. Bingefors et al., Nucl. Instr. and Meth. A 328 (1993) 447.
[3] H.-G. Moser, Nucl. Instr. and Meth. A 310 (1991) 490.
[4] C. Adolphsen et al., Nucl. Instr. and Meth. A 313 (1992) 63.
[5] P. Weilhammer and R. Turchetta, private communication.
[6] L. Hubbeling et al., Nucl. Instr. and Meth. A 310 (1991) 197.
[7] R. Brenner et al., Nucl. Instr. and Meth. A 326 (1993) 189.
[8] H. Tajima et al., Nucl. Instr. and Meth. A 310 (1991) 504.
[9] H. Hanai et al., Nucl. Instr. and Meth. A 314 (1992) 455.
[10] The DELPHI Collaboration, DELPHI 92-142 GEN 235 (1992).
[11] J. Hylen et al., Nucl. Instr. and Meth. A 310 (1991) 497.
[12] RD20 Proposal, CERN/DRDC 91-10, DRDC/P26 (1991).
[13] E. Gatti and P.F. Manfredi, Nuovo Cimento 9 ser. 3 (1986).
[14] P. Cattaneo, Nucl. Instr. and Meth. A 295 (1990) 207.
[15] H. Ikeda, M. Tanaka and S. Okuno, Nucl. Instr. and Meth. A 313 (1992) 31.
[16] M. Caccia et al., Nucl. Instr. and Meth. A 260 (1992) 124.
[17] U. Kotz et al., Nucl. Instr. and Meth. A 235 (1985) 282.
[18] V. Radeka and R.A. Boie, Nucl. Instr. and Meth. 178 (1980) 543.
[19] E. Belau et al., Nucl. Instr. and Meth. 214 (1983) 253.
[20] G. Batignani et al., IEEE Trans. Nucl. Sci. NS-36 (1) (1989) 40.
[21] C.J.S. Damerell, RAL-84-123 (1984).
[22] H. Bichsel, Rev. Mod. Phys. 60 (3) (1988) 663.
[23] W. Snoeys et al., Nucl. Instr. and Meth. A 326 (1993) 144.